Review of Scientific Instruments

A steady-state thermoreflectance method to measure thermal conductivity

Cite as: Rev. Sci. Instrum. **90**, 024905 (2019); https://doi.org/10.1063/1.5056182
Submitted: 12 September 2018 . Accepted: 09 February 2019 . Published Online: 28 February 2019

Jeffrey L. Braun, David H. Olson, John T. Gaskins, and Patrick E. Hopkins

AIP Publishing

Review of Scientific Instruments ARTICLE scitation.org/journal/rsi

A steady-state thermoreflectance method to measure thermal conductivity

Cite as: Rev. Sci. Instrum. 90, 024905 (2019); doi: 10.1063/1.5056182
Submitted: 12 September 2018 • Accepted: 9 February 2019 •
Published Online: 28 February 2019

Jeffrey L. Braun,[1] David H. Olson,[1] John T. Gaskins,[1] and Patrick E. Hopkins[1,2,3,a)]

AFFILIATIONS

[1]Department of Mechanical and Aerospace Engineering, University of Virginia, Charlottesville, Virginia 22904, USA
[2]Department of Materials Science and Engineering, University of Virginia, Charlottesville, Virginia 22904, USA
[3]Department of Physics, University of Virginia, Charlottesville, Virginia 22904, USA

[a)]**Electronic mail:** phopkins@virginia.edu

ABSTRACT

We demonstrate a steady-state thermoreflectance-based optical pump-probe technique to measure the thermal conductivity of materials using a continuous wave laser heat source. The technique works in principle by inducing a steady-state temperature rise in a material via long enough exposure to heating from a pump laser. A probe beam is then used to detect the resulting change in reflectance, which is proportional to the change in temperature at the sample surface. Increasing the power of the pump beam to induce larger temperature rises, Fourier's law is used to determine the thermal conductivity. We show that this technique is capable of measuring the thermal conductivity of a wide array of materials having thermal conductivities ranging from 1 to >2000 W m^{-1} K^{-1}, in excellent agreement with literature values.

I. INTRODUCTION

Measurement techniques used to characterize the thermal conductivity (κ) of materials can be broadly categorized into steady-state and transient techniques. The former, based on Fourier's law, allow for direct measurements of thermal conductivity, whereas the latter rely on the heat diffusion equation such that volumetric heat capacity and thermal conductivity are coupled through the thermal effusivity or thermal diffusivity, depending on the time and length scales of the measurement. Some examples of transient techniques include transient hot-wire,[1] transient plane source,[2] the 3ω method,[3] and non-contact pump-probe techniques such as laser flash,[4] time-domain thermoreflectance (TDTR),[5] and frequency-domain thermoreflectance (FDTR).[6] The 3ω method, TDTR, and FDTR have proven to be robust techniques capable of measuring thermal properties of both bulk and thin film materials. TDTR and FDTR, specifically, have the advantage of being non-contact techniques requiring a very small experimental surface area to heat and probe. However, these techniques can be expensive and difficult to operate as they generally require detection of the phase shift of a signal that needs to be separated from instrument electronic phase shifts along with additional knowledge of the heat capacity of the material under study.

Steady-state techniques include the absolute technique, the comparative cut bar technique, the radial heat flow method, and the parallel thermal conductance technique. Zhao *et al.* provide an extensive review of these techniques.[7] While these techniques are straightforward and require only variations of Fourier's law to analyze experimental data, they have practical limitations that make them undesirable compared to the aforementioned transient techniques. For example, all of these techniques are designed for bulk materials, so they require relatively large experimental volumes and heater/sensor areas. This makes them highly susceptible to radiative and convective losses, often necessitating vacuum conditions during measurements.[8] Moreover, techniques requiring contact between a sensor and a sample generally include the undesired artifact of contact thermal resistance that can obscure the measurement of intrinsic thermal conductivity. Additionally, they can require waiting times up to several hours to reach steady-state temperatures. Finally, these techniques fundamentally measure the thermal conductance across a bulk specimen rather than within a locally probed area as has been shown in FDTR[9,10] and

TDTR.[11,12] Given the benefits inherent in transient pump-probe techniques and the simplicity of steady-state techniques, we develop a steady-state thermoreflectance (SSTR) technique based on a continuous wave (CW) laser pump and probe. We show that SSTR is robust, capable of measuring materials having thermal conductivities ranging from 1 to >2000 W m^{-1} K^{-1}, showing excellent agreement with literature values.

SSTR has several key benefits over conventional steady-state techniques. First, because transient temperature rise times can be on the order of tens of microseconds, SSTR is capable of high throughput measurements, limited only by the electronics and sampling periods used. Typical measurement times in this study vary from about 10 s to 5 min per scan depending on the resolution needed. Second, SSTR is non-contact, requiring no attached thermocouple. Akin to TDTR and FDTR, SSTR as presented in this work is facilitated with the deposition of a thin metal film transducer. However, because the time scales associated with SSTR measurements (i.e., >tens of microseconds) can be much longer than lifetimes of photoexcited carriers that can also contribute to changes in reflectivity, an additional transducer may not be needed.[13,14] Third, steady-state techniques generally require large thermal resistances for accurate measurements so that the minimum sample volume needed scales with the sample's thermal conductivity. By contrast, the thermal penetration depth in SSTR is governed solely by the pump radius since this radius determines the thermal penetration depth in steady-state laser heating.[15] As such, the measurement volume of SSTR is independent of the thermal properties of the material under study; we show this later by measuring 300 μm thick wafers of diamond. Furthermore, because the thermal length scales are governed by the pump radius, the spatial resolution in SSTR is limited only by the ability to focus the pump and probe; in our experiments, we can obtain pump/probe $1/e^2$ radii as low as ~1 μm. This allows us to probe local thermal conductivities to avoid, for example, damaged regions of a bulk specimen that could otherwise obscure the intrinsic thermal conductivity. Additionally, this allows for measurements of moderately thick films ranging from tens to hundreds of microns without significant influence of any underlying substrate.

Comparing SSTR to transient thermoreflectance techniques, SSTR has a few distinct advantages. First, TDTR and FDTR generally have shallow thermal penetration depths (<1 μm for most materials), so they are typically mostly sensitive to cross-plane thermal conductivity. By comparison, SSTR is fundamentally sensitive to the determinant of the total thermal conductivity tensor, analogous to the 3ω method.[16] Second, when a thin film transducer is used, generally, the large thermal penetration depth makes the temperature rise at the sample surface more sensitive to the thermal properties of the sample rather than the transducer properties or interface resistances. Third, since there is no time dependence after the transient rise time, the steady-state temperature profile is solely dependent on thermal conductivity. From a practical point of view, this greatly simplifies the experiment and analysis.

II. PRINCIPLES OF OPERATION

Detection of reflectivity (R) changes due to an induced temperature (T) rise is limited by the very small relative change in reflectivity of a material with temperature. For typical metals used as transducers in thermoreflectance experiments, $|dR/dT|$ is on the order of 10^{-5} or 10^{-4} K^{-1}.[17–19] There are two ways by which this limitation can be overcome. Using a periodic heat source, lock-in amplification (LIA) techniques overcome this limitation through amplification and electronic filtering. Similarly, a periodic waveform analyzer (PWA) with a boxcar averager can be used with a large enough sampling time to extract a periodic signal. Since the steady-state signal has no frequency component, we seemingly cannot use these techniques to measure the $|dR/dT|$ associated with the "DC" temperature rise. Generally, in steady-state techniques, a constant heat flux is used to induce a transient temperature rise followed by a steady-state temperature rise. The transient portion of the temperature rise, which can persist for hours in bulk techniques,[7] is ignored, and measurements are taken only in the steady-state regime. In SSTR, obtaining a fast transient temperature rise followed by a long-lived steady-state temperature rise allows us to cyclically turn the steady-state temperature rise on and off, enabling use of the aforementioned signal detection schemes.

Thus, the concept of SSTR is to modulate the pump beam with a square wave at a low enough frequency to enable an "on" state and an "off" state for the steady-state temperature rise to be reached. By varying the power ($\propto$ heat flux) of the pump beam, we can vary the temperature rise of the "on" state. Measuring the corresponding change in reflectivity ($\propto$ temperature), we can apply Fourier's law to determine thermal conductivity based on the linear relation between heat flux and temperature. This concept is fundamentally different from FDTR in that our controlled variable is pump power and we rely on measuring the magnitude of the reflectance signal, which is directly proportional to the temperature rise induced by the pump under steady-state temperature rise conditions. As such, there is no need to separate the electronic phase from the overall signal phase, as is necessary in both TDTR and FDTR.

III. THEORY

A. Transient temperature rise

We now establish the criteria needed to establish a steady-state temperature rise "on" state. To do this, we solve the heat diffusion equation in the time-domain to determine the time needed for the temperature rise to reach steady-state. Using the radially symmetric heat diffusion equation, a material at an initial temperature rise of zero degrees at time $t = 0$ is subjected to a temporally constant, spatially Gaussian heat flux at the sample surface to simulate CW laser heating. A semi-infinite boundary condition is applied in all spatial dimensions. The derivation for this solution is provided in Appendix A. We find that two experimental parameters can be balanced to determine the operating conditions needed to achieve a steady-state: the pump/probe radius

and the modulation frequency of the pump. This can be seen in two common examples used as calibrations in TDTR and FDTR, silicon (Si, $\kappa \approx 140$ W m^{-1} K^{-1}) and amorphous silicon dioxide (a-SiO$_2$, $\kappa \approx 1.4$ W m^{-1} K^{-1}). For simplicity, these thermal conductivities were approximated to be exactly 100× different from one another. Three $1/e^2$ pump/probe diameters spanning three orders of magnitude are considered: 1, 10, and 100 μm. Pump and probe sizes are equal in all example cases. Figure 1 shows the normalized temperature rise, $\Delta T/\Delta T_{SS}$, where $\Delta T_{SS} = \Delta T(t \rightarrow \infty)$ is the steady-state temperature rise, shown for (a) Si and (b) a-SiO$_2$. Since thin metal transducers are typically used in experiments, we apply the solution both with and without an 80 nm aluminum (Al) layer.

Strictly speaking, the temperature rise asymptotes to the steady state temperature rise, but we can define a threshold for $\Delta T/\Delta T_{SS}$ based on a desired measurement tolerance. For example, if a ratio of 95% is used, we can select a modulation frequency that has a period longer than the 95% rise time of the temperature rise. For Si, the 95% rise times for a $1/e^2$ pump diameter of 1, 10, and 100 μm are ~10^{-7}, 10^{-5}, and 10^{-3} s, respectively. Similarly, for a-SiO$_2$, the 95% rise times for a pump radius of 1, 10, and 100 μm are ~10^{-5}, 10^{-3}, and 10^{-1} s, respectively. It is instructive to compare Si to a-SiO$_2$, which differ in thermal diffusivity by almost exactly two orders of magnitude. We see that for the same pump diameter, the rise time of a-SiO$_2$ is two orders of magnitude longer than for Si. Furthermore, for both Si and a-SiO$_2$, increasing the pump diameter by one order of magnitude increases the rise time by exactly two orders of magnitude. These two correlations suggest we can use the nondimensional Fourier number, Fo $= \alpha t/r_0^2$, where α is the thermal diffusivity, t is time, and r_0 is the pump radius, to generalize these results for a universal criterion to determine the rise times for any material. Figure 1(c) shows the relation between $\Delta T/\Delta T_{SS}$ and Fo, which holds true for any material having the previously defined boundary conditions.

As previously mentioned, thermoreflectance experiments generally require use of a thin metal transducer. In addition to having significant impact on the steady-state temperature rise itself,[20] we find that it can have significant impact on the rise time of the transient temperature rise. For example, for 80 nm Al/Si, the rise time is lower than it is without the transducer layer for all laser spot sizes, allowing for higher modulation frequencies to be used to obtain a steady-state temperature rise. Conversely, the addition of an 80 nm Al layer to a-SiO$_2$ leads to longer 95% rise times than without the transducer layer. However, in both cases, the degree to which the rise time differs from the predictable case without this transducer is entirely dependent on the pump spot size, relative mismatch in thermal properties between the transducer layer and the substrate, and, to a lesser extent, the thermal boundary conductance between the transducer and the substrate. In particular, as laser spot size decreases, the influence of the transducer on the rise time becomes more substantial. Still, we find that in most cases, the nondimensional relation found in Fig. 1(c) is a useful guide to select the maximum modulation frequency, given the pump radius and a rough idea of

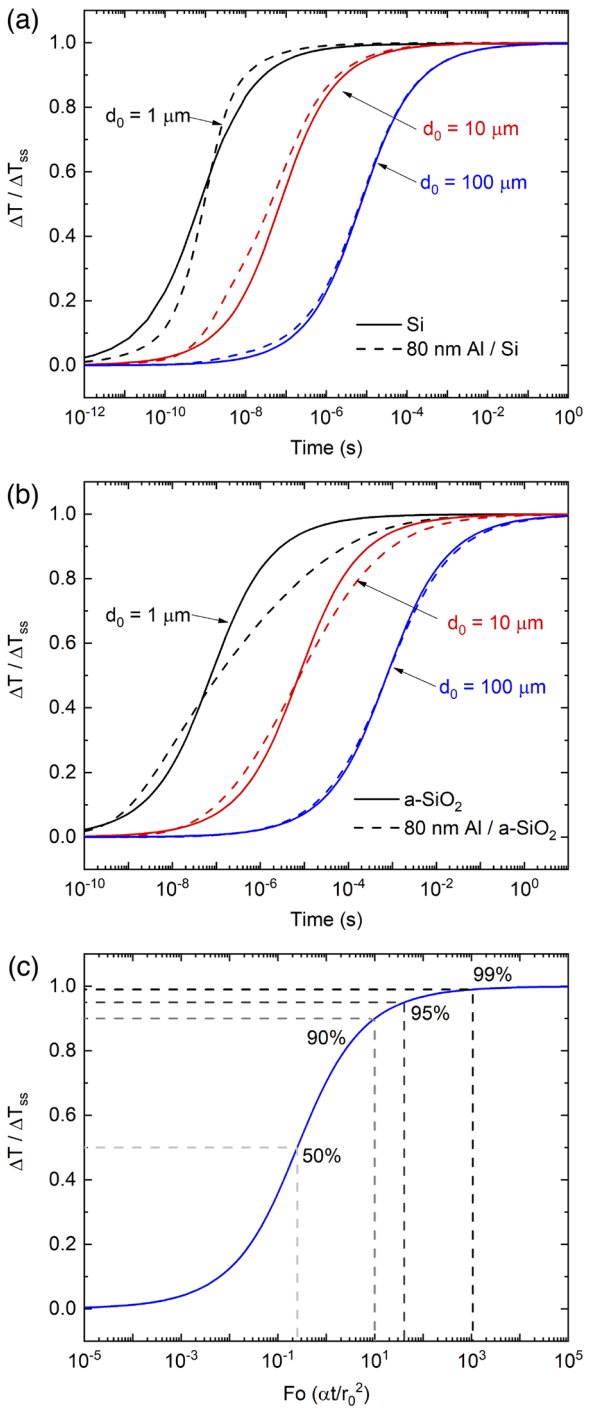

FIG. 1. Normalized surface temperature rise ($\Delta T/\Delta T_{SS}$) vs. time for (a) Si and (b) a-SiO$_2$ for CW laser surface heating with $1/e^2$ diameters (d_0) of 1 μm, 10 μm, and 100 μm. Solid lines indicate no transducer, while dashed lines show the case with an 80 nm Al transducer. (c) $\Delta T/\Delta T_{SS}$ vs. Fourier number in the case of no transducer. Thermal parameters used in the model include those for a-SiO$_2$ (C_v = 1.66 MJ m^{-3} K^{-1}, κ = 1.4 W m^{-1} K^{-1}), Si (C_v = 1.60 MJ m^{-3} K^{-1}, κ = 140 W m^{-1} K^{-1}), and Al (C_v = 2.42 MJ m^{-3} K^{-1}, κ = 130 W m^{-1} K^{-1}). Thermal boundary conductance between Al and substrate was modeled to be 200 MW m^{-2} K^{-1}.

the thermal diffusivity of a sample. Of course, in practice, one can simply select a modulation frequency as low as possible to ensure that the steady-state temperature rise is reached; the advantage of using higher modulation frequencies, if possible, is to reduce $1/f$ noise and expedite testing times.

B. Quasi steady-state via a sine wave heat source

While the theoretical discussion thus far has been based on the idea of inducing an on/off state of the steady-state temperature rise (i.e., square wave modulation), many lock-in amplifiers use a pure sinusoid as a reference mixer such that higher harmonics are not captured in detection. In this case, the lock-in only captures the magnitude of the probe signal at the fundamental frequency of the square wave. This does not pose an experimental problem, however, as we can still obtain a regime of quasi steady-state temperature rise. To illustrate this point, we examine the frequency-domain solution to the heat equation subjected to CW laser heating with a sinusoidal amplitude modulation.[6] The normalized temperature rise, $\Delta T/\Delta T_{SS}$, is shown in Fig. 2 for a-SiO_2, crystalline sapphire (Al_2O_3), Si, and diamond with 80 nm Al transducers. The solutions are shown for $1/e^2$ pump and probe diameters of 1 μm, 10 μm, and 100 μm in Figs. 2(a)–2(c), respectively. The temperature rise ΔT is the modulated temperature rise that varies sinusoidally at the same frequency as the laser heat source, but its magnitude asymptotes to a constant value, that of the steady-state temperature rise, as the modulation frequency approaches zero. Similar to the transient temperature rise case discussed previously, we see that smaller laser spot sizes allow for a quasi steady-state temperature rise to be reached at higher modulation frequencies. We can exploit this fact by running experiments at higher modulation frequencies and smaller spot sizes to reduce $1/f$ noise at low frequencies.

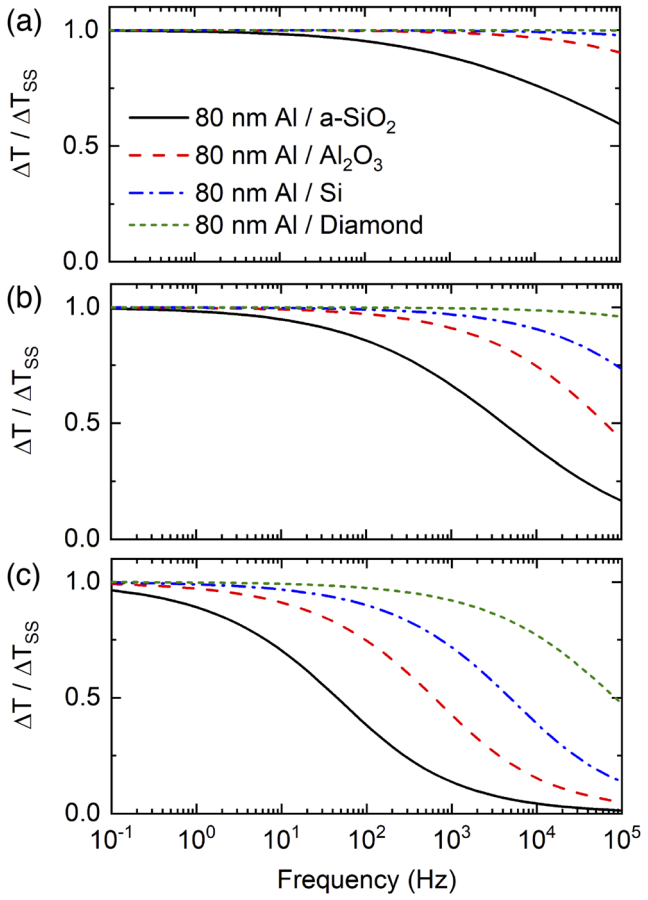

FIG. 2. Normalized surface temperature rise ($\Delta T/\Delta T_{SS}$) vs. modulation frequency for CW laser heating with an amplitude modulated sinusoidal profile. The samples modeled include a-SiO_2 (C_v = 1.66 MJ m^{-3} K^{-1}, κ = 1.4 W m^{-1} K^{-1}), Al_2O_3 (C_v = 3.06 MJ m^{-3} K^{-1}, κ = 35 W m^{-1} K^{-1}), Si (C_v = 1.60 MJ m^{-3} K^{-1}, κ = 140 W m^{-1} K^{-1}), and diamond (C_v = 1.78 MJ m^{-3} K^{-1}, κ = 2000 W m^{-1} K^{-1}), shown for pump and probe $1/e^2$ diameters of (a) 1 μm, (b) 10 μm, and (c) 100 μm. Al was modeled to have C_v = 2.42 MJ m^{-3} K^{-1} and κ = 130 W m^{-1} K^{-1}, while Al/substrate thermal boundary conductance was modeled as 200 MW m^{-2} K^{-1} in all cases.

IV. EXPERIMENTAL DETAILS

Our experimental setup, shown in Fig. 3, consists of a CW diode probe laser (Coherent Cube), having a wavelength of 786 nm and output power up to 30 mW, and a CW pump laser (Spectra-Physics Millenia Vs) with a wavelength of 532 nm and output power up to 5 W. In practice, the pump power is limited to <200 mW except in the case of the most conductive materials studied here, where output powers up to 1 W proved sufficient for the pump radii used in this study. Likewise, the probe output is limited to <1 mW to avoid any additional heating of the sample. A mechanical chopper (Thorlabs MC2000B) is used to modulate the pump. Identical experiments were performed using an electro-optic modulator (Thorlabs EO-AM-NR-C4) with excellent agreement found between the two modulation sources. Ultimately, the chopper is preferred because it is simple to use, is inexpensive, allows for fully on/off square waves, and has a damage threshold far exceeding the operating powers of the pump. Internal modulation of a pump laser offers a further step toward simplicity and cost reduction of the SSTR system. The pump waveform and power are monitored by using a photodetector (Thorlabs DET10A) by picking off 10% of the beam using a 90:10 beam splitter. Although a power meter is sufficient for this purpose and was used in our original implementation of SSTR, a photodetector is preferable because it allows us to send the signal to a second oscillator in the lock-in amplifier to measure the pump power in the same way we do the probe, i.e., with LIA or PWA detection. A neutral density (ND) filter is placed before the pump photodetector to avoid saturation of the detector. The transmitted power is then reflected by a cold mirror and sent through an objective lens to focus onto the sample.

The probe is split into two paths using a polarizing beam splitter. A half-wave plate is used to control the power of each path. The transmitted portion is used as a reference, while the reflected portion passes through a quarter-wave plate that is adjusted to allow for maximum transmission of the back-reflected probe from the sample. The probe is transmitted through the cold mirror and is focused coaxially with the

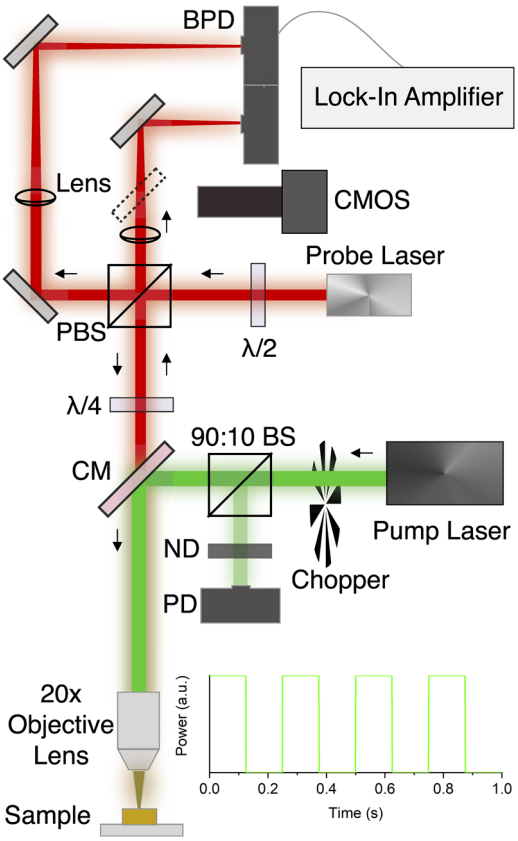

FIG. 3. Schematic of the Steady-State Thermoreflectance (SSTR) experiment. PBS: polarizing beam splitter, $\lambda/2$, $\lambda/4$: half- and quarter-wave plates, respectively, 90:10 BS: 90% transmission/10% reflection beam splitter, PD: photodetector, BPD: balanced photodetector, ND: neutral density filter. The inset shows a representative pump waveform vs. time.

pump onto the sample using an objective lens. The focused pump and probe diameters were adjusted with lenses to be equivalent sizes. Using 20× and 10× objective lenses, the $1/e^2$ diameters are 11 μm and 20 μm, respectively, as measured via a scanning slit beam profiler (Thorlabs BP209-VIS). The probe is back-reflected to a balanced photodetector (Thorlabs PDB410A) along with the path-matched reference beam to minimize common noise in the probe. The powers of the reference and sample beams going into the photodetector are adjusted to be equivalent via the half-wave plate to minimize noise. Samples tested in this study include two types of a-SiO_2, a plain glass microscope slide (Fisherbrand) and a 3 mm thick borosilicate glass (BK7) optical window (Thorlabs WG10530); a 1 mm thick quartz wafer (Precision Micro Optics); two types of Al_2O_3, a 300 μm thick wafer (UniversityWafer) and a 3 mm thick window (Thorlabs WG30530); two types of Si, a 300 μm thick wafer (UniversityWafer) and a 3 mm thick window (Thorlabs WG80530); a 300 μm thick nitrogen-doped, n-type 4H–silicon carbide (4H–SiC) wafer (MTI Corporation); and a 300 μm thick polycrystalline diamond wafer (Element Six TM200).

When using the 10× objective lens, we typically use a higher order ND filter to further reduce power going into the pump photodetector. This is done to compensate for the increased power needed to heat the sample to similar temperatures to those achieved with the 20× objective. Using a lock-in amplifier (Zurich Instruments UHFLI) synced to the chopper frequency, the magnitude (ΔV) of the probe signal divided by the DC probe signal (V) is recorded simultaneously with the lock-in magnitude of the pump photodetector (ΔP). ΔP as determined by the LIA is proportional to the amplitude of the sinusoidal component of the pump waveform. Likewise, ΔV corresponds to only the sinusoidal component of the probe waveform. LIA detection thus allows for modulation of the pump with an arbitrary periodic waveform (square, sine, triangle, etc.) and with any offset power to obtain the same relation between the lock-in pump power and the lock-in probe magnitude. The pump power is increased linearly so that a linear relation between $\Delta V/V$ with pump power is obtained. The slope of this relation, after determining the appropriate proportionality constant, is used to determine thermal conductivity by comparing it to the thermal model given in Appendix B. Alternatively, a PWA with a boxcar averager is used to record both the pump and probe waveforms over several periods of temperature oscillation by again syncing to the chopper frequency. Using this approach, we can visualize the sample temperature rise vs. time to determine the steady-state regime of the temperature rise.

Comparing the two detection schemes, the LIA approach allows for faster data acquisition, allows for full automation of both data acquisition and analysis, and is independent of the waveform used as only the sinusoidal component is recorded. However, because sinusoidal modulation can only achieve a quasi steady-state, for accurate determination of low-diffusivity materials, (i) the modulation frequency must be lower compared with the PWA case or (ii) the thermal model must include the modulation frequency as an input parameter. The PWA approach, on the other hand, extracts the total waveform of the probe reflectivity vs. time. As such, the square wave reflectivity waveform that results from a square wave pump input can be deduced. Furthermore, data analysis is performed by manually choosing the time range in which the "on" and "off" state occur, ensuring we can pick the true steady-state temperature rise for determining thermal conductivity.

V. SIGNAL ANALYSIS

The probe reflectivity response measured by using the photodetector, $\Delta V/V$, is proportional to the normalized change in reflectivity, $\Delta R/R$, which is related to the change in temperature of the sample surface by the thermoreflectance coefficient β so that

$$\frac{\Delta R}{R} = \left(\frac{1}{R}\frac{\partial R}{\partial T}\right)\Delta T = \beta\,\Delta T. \tag{1}$$

In general, β is temperature dependent. For Al, β is 1.14×10^{-4} K^{-1} and varies at a rate of $0.22 \times 10^{-4}/100$ K[21] near our probe wavelength of 786 nm. Keeping temperature

rises below 50 K ensures β varies less than 10%; estimated temperature rises[20] for our experiments are <20 K. Using the thermoreflectance coefficient and an additional conversion of $\Delta V/V$ to $\Delta R/R$, we can obtain ΔT. Next, by measuring the power of the pump and the reflectance of the sample at the pump wavelength, we can in principle calculate the heat flux absorbed by the sample. These two quantities allow for the determination of thermal conductivity through Fourier's law applied to a semi-infinite substrate. Thus, accurate determination of heat flux and temperature would allow for an absolute technique to directly measure thermal conductivity. Since we measure $\Delta V/V$ and the pump photodetector response, $\Delta P \propto$ pump power, we seemingly have two proportionality constants to consider, one relating $\Delta V/V$ to ΔT and one relating ΔP to the heat flux magnitude $\Delta|Q|$. We eliminate one of these proportionality constants by determining $\Delta V/(V\,\Delta P)$ so that

$$\left(\frac{\Delta V}{V\,\Delta P}\right) = \gamma\left(\frac{\Delta T(\kappa)}{\Delta|Q|}\right), \tag{2}$$

where $\Delta T/\Delta|Q|$ is calculated using the thermal model presented in Appendix B. Next, we use a calibration, with a known thermal conductivity, to determine γ,

$$\gamma = \left(\frac{\Delta T(\kappa_{cal})}{\Delta|Q|}\right)^{-1}_{cal}\left(\frac{\Delta V}{V\,\Delta P}\right)_{cal}. \tag{3}$$

The calibration used to determine γ is a single-crystal sapphire (Al_2O_3) wafer, measured to have a net thermal conductivity ($\sqrt{\kappa_r\kappa_z}$) of 35 ± 2 W m^{-1} K^{-1} using both time-domain thermoreflectance and a hot-disk transient plane source technique (Hot Disk AB TPS 3500). We determine γ by comparing the measured $\Delta V/(V\,\Delta P)$ to the ΔT predicted using the thermal model. We note that γ is different for different objective lenses used because (i) power loss may not be the same within the two objectives and (ii) we use a stronger neutral density filter to reduce power detected with the pump photodetector when moving from the 20× to 10× objective to avoid saturation of the detector. Additionally, γ will differ between the LIA and the PWA approaches.

With γ defined by a calibration, the measurement of $\Delta V/(V\,\Delta P)$ for any sample can be related to the sample's thermal conductivity by relating it to a thermal model predicting $\Delta T(\kappa)/\Delta|Q|$. The thermal conductivity input to the model is adjusted to obtain the best fit to the experimental data using a global minimization algorithm to search for the smallest absolute difference between the model and the data. The fundamental assumption using this approach is that the proportionality constant γ, which encompasses the thermoreflectance coefficient and conversion factor of change in reflectance to change in photodetector voltage, is equivalent between the calibration and the sample. To ensure this, we evaporate an 80 nm Al transducer layer on all samples under the same deposition to ensure that the thermoreflectance coefficient is the same from sample to sample. As a general rule, we adjust the input power of the pump to induce approximately the same magnitude of $\Delta V/V$ for each sample. This ensures that any nonlinear responses, whether from physical parameters such as the thermoreflectance coefficient or from the photodetector response, however small, are offset since they are encompassed in γ.

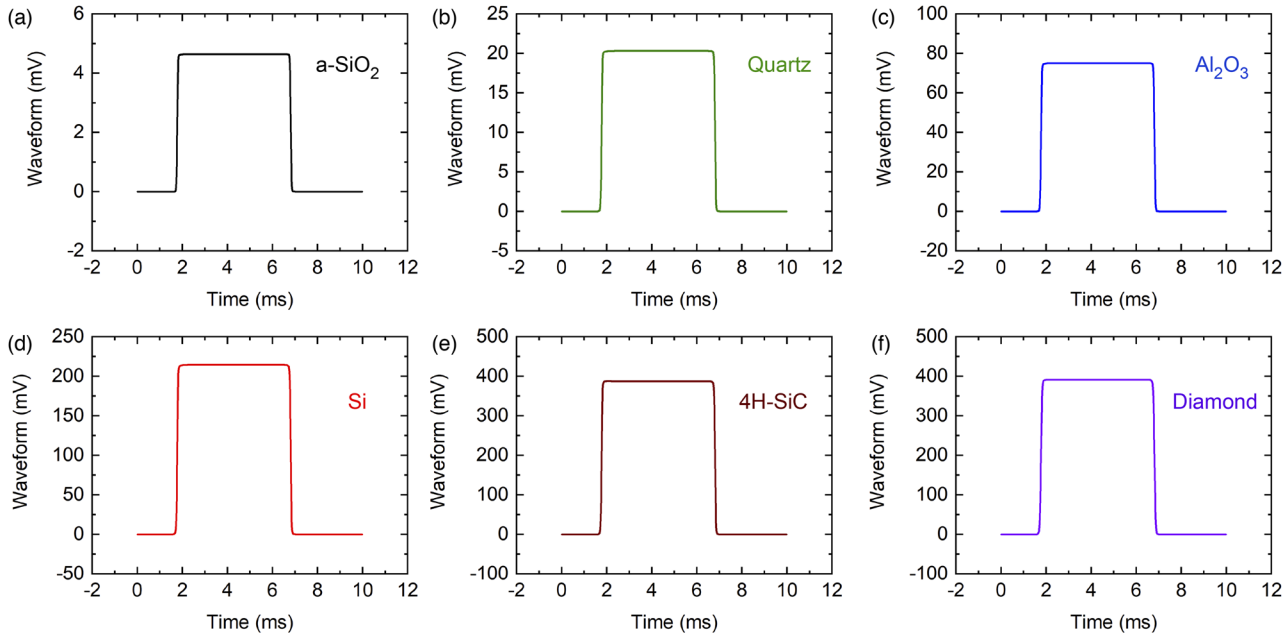

FIG. 4. Pump waveforms obtained using a periodic waveform analyzer, shown for (a) *a*-SiO_2, (b) quartz, (c) Al_2O_3, (d) Si, (e) 4H–SiC, and (f) diamond. The difference between the upper and lower regimes of the waveform magnitude, ΔP (proportional to heat flux), is used to determine thermal conductivity in each case.

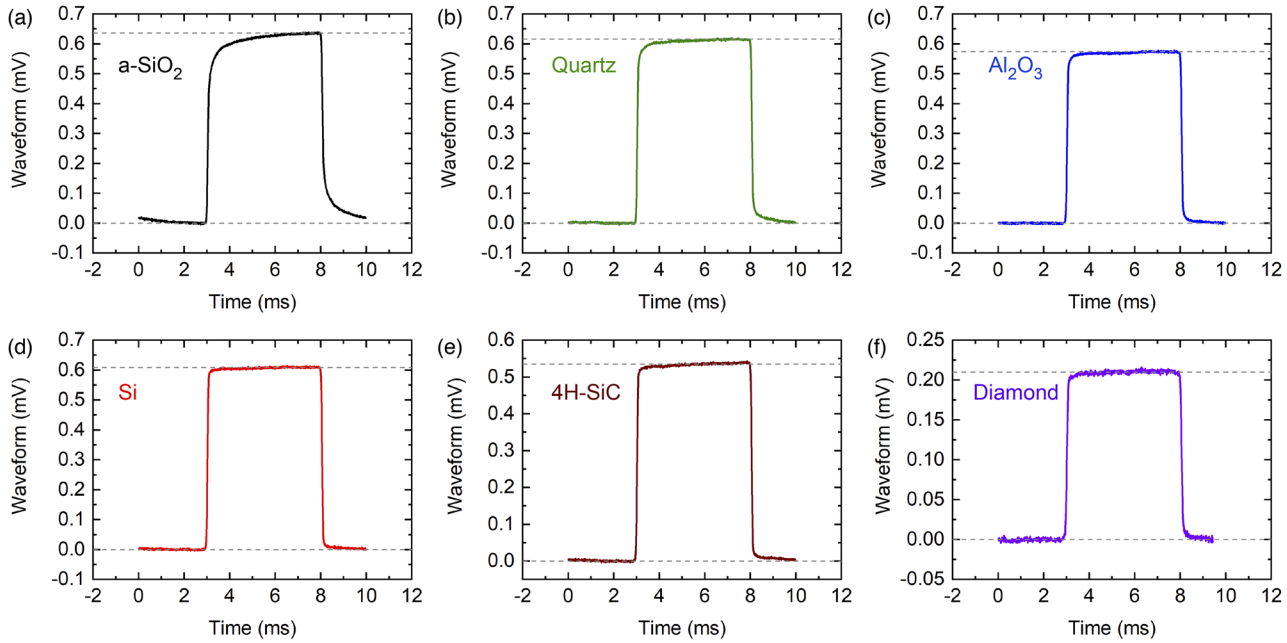

FIG. 5. Probe waveforms obtained using a periodic waveform analyzer, shown for (a) *a*-SiO_2, (b) quartz, (c) Al_2O_3, (d) Si, (e) 4H–SiC, and (f) diamond. The difference between the upper and lower dashed lines indicates the ΔV (proportional to temperature rise) used to determine thermal conductivity in each case.

A. Periodic waveform analyzer/boxcar averager

We first collect data using the PWA via a digital boxcar averager while modulating the pump beam with a chopper at 100 Hz. Using two independent oscillators, we simultaneously record the pump and probe waveforms over a phase space divided into 1024 bins. The reference frequency is provided by the chopper. The resulting waveforms, which have been converted from phase space to time, are shown for the pump in Fig. 4, while those of the probe are shown in Fig. 5. The six samples shown include (a) an *a*-SiO_2 glass slide, (b) z-cut quartz, (c) Al_2O_3, (d) Si, (e) 4H–SiC, and (f) diamond. The modulation frequency was kept at 100 Hz in all cases, and a 20× objective lens was used, corresponding to $1/e^2$ pump/probe diameters of 11 μm. Each waveform was generated by averaging over 5 min of real time data acquisition.

As expected, the pump waveform shows a perfect on/off square wave. Note that the magnitude is increased when moving to higher thermal conductivity materials to allow for the probe waveform to reach approximately the same magnitude in each sample. The probe waveforms reveal that for all samples except *a*-SiO_2, a clear steady-state temperature rise is obtained as indicated by the near-square waveform. By comparison, *a*-SiO_2 has a relatively long-lived transient temperature rise but reaches our steady-state threshold by the end of the waveform. The advantage of PWA analysis is that the signal difference between "on" and "off" state (ΔV) is chosen manually so that we can neglect the transient portions of the

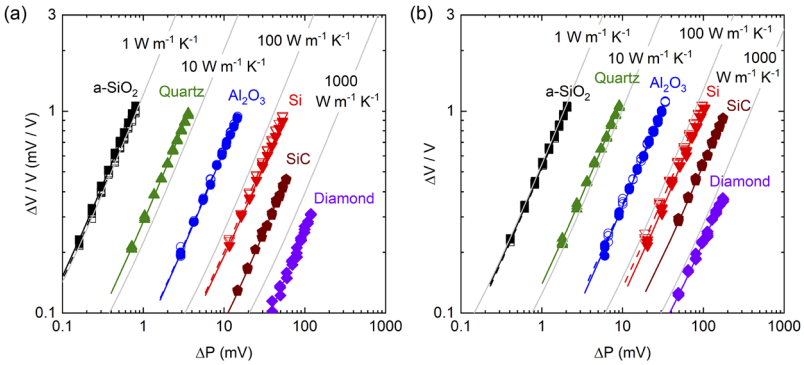

FIG. 6. Measured $\Delta V/V$ vs. ΔP ($\propto$ pump power) shown for (a) 10× objective lens (pump and probe $1/e^2$ diameters of 20 μm) and (b) 20× objective lens (pump and probe $1/e^2$ diameters of 11 μm). Measured samples include glass slide (squares), BK7 glass (open squares), quartz (triangles), sapphire wafer (circles), sapphire window (open circles), silicon wafer (inverted triangles), silicon window (open inverted triangles), 4H–SiC (pentagons), and diamond (diamonds). Gray lines show the predicted slopes for materials having thermal conductivities 1, 10, 100, and 1000 W m^{-1} K^{-1}. A different neutral density filter was used to filter pump power detected when the objective lens changed from 10× to 20×, so the x-axes are not comparable between (a) and (b).

temperature rise (however small) and only extract the steady-state regime. This is achieved through a MATLAB script in which we pick the range of time to extract signal in the "on" state and "off" state and subtract the mean signal of each state. The difference corresponds to ΔV. The mean "on" and "off" signals chosen for each case are displayed as dashed lines in Fig. 5. We repeat the same process for the pump waveform, where the difference between high and low waveform states corresponds to ΔP. With γ defined using a calibration, this is all the information we need to determine thermal conductivity via a purely steady-state model (i.e., modulation frequency = 0 in the model).

B. Lock-in amplifier

Next, we collect data via the LIA. To do so, we use the chopper reference frequency to lock into the periodic signal produced by the reflected probe. Using an automated program to control the pump power via serial command, we capture the magnitude of probe lock-in voltage as a function of 10 powers. Figure 6 shows the resulting relationship between ΔV/V and proportional pump power (ΔP) for two objective lenses, 10× and 20×. The lock-in time constant used was 400 ms and each datapoint represents the average over ~10 s of acquisition. The data shown include those from 3 to 5 spots on each sample, which is the primary reason for any visible noise observed. Each 10-data point scan takes about 2 to 3 min to run; this time is primarily dictated by the wait time allowed to adjust the pump power. However, in principle, after characterizing the noise floor, only a single data point is needed to establish a slope suggesting the data acquisition time is limited only by the time to reach a steady lock-in magnitude.

A linear fit is performed on each dataset to determine the slope, ΔV/(V ΔP). From this, the thermal conductivity can be determined by comparing this slope to the thermal model after dividing by γ. Figure 6 shows the expected slopes for a material having thermal conductivity of 1, 10, 100, and 1000 W m^{-1} K^{-1}. Comparing these lines with our experimental data, we see that our samples' slopes fall in line with what is expected for each substrate. For these models, we assumed an Al transducer thermal conductivity that is descriptive of what we measure via four point probe resistivity measurements, ~100 W m^{-1} K^{-1}, a constant thermal boundary conductance of 200 MW m^{-2} K^{-1}, and modulation frequency of 100 Hz. To determine the impact of these assumptions, we need to determine sensitivity to our model parameters, described below.

C. Parameter sensitivity

We quantify the sensitivity, S_x, of the thermal model to parameter x using a similar approach to that defined by Yang *et al.*[9] by varying x plus or minus 10%. Since we measure the magnitude instead of phase, we add an additional division term to allow for fair comparison of sensitivities between samples. Thus,

$$S_x = \frac{|\Delta T_{1.1x}(r_{01}) - \Delta T_{0.9x}(r_{01})|}{\Delta T_x(r_{01})}, \quad (4)$$

where ΔT_x is the temperature rise calculated for the input parameter x and $r_{01} = \sqrt{r_0^2 + r_1^2}$, where r_0 and r_1 are the pump and probe radii, respectively. We define sensitivity as a function of r_{01} to show that we gain sensitivity to different parameters by utilizing multiple pump/probe diameters. Figure 7 shows the sensitivity as a function of r_{01} for four parameters, in-plane transducer thermal conductivity ($\kappa_{r,1}$), transducer thickness (d_1), sample thermal conductivity ($\kappa_2 \equiv \sqrt{\kappa_{r,2}\kappa_{z,2}}$), and thermal boundary conductance (G) between the transducer and the substrate. The r_{01} used in our experiments are shown as dashed lines. Three samples are considered: (a) a-SiO_2, (b) Al_2O_3, and (c) diamond. Amorphous silica and diamond were chosen to display because they represent the lower and upper extremes of thermal conductivity

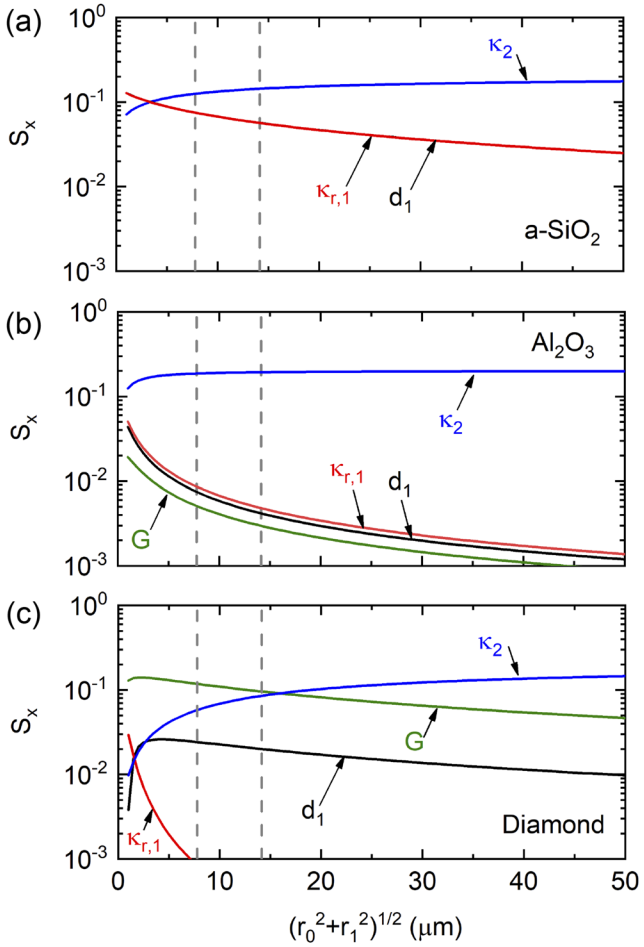

FIG. 7. Sensitivity, S_x, to parameter x vs. effective radius, defined as $\sqrt{r_0^2 + r_1^2}$, where r_0 and r_1 are the pump and probe radii, respectively, shown for (a) a-SiO_2, (b) Al_2O_3, and (c) diamond. S_x is defined by Eq. (4) and the parameters varied include the sample thermal conductivity, κ_2; the transducer in-plane thermal conductivity, $\kappa_{r,1}$; transducer thickness, d_1; and the thermal boundary conductance, G, between the sample and the transducer. κ_2 is defined as the geometric mean of the cross- and in-plane thermal conductivities, $\sqrt{\kappa_z \kappa_r}$.

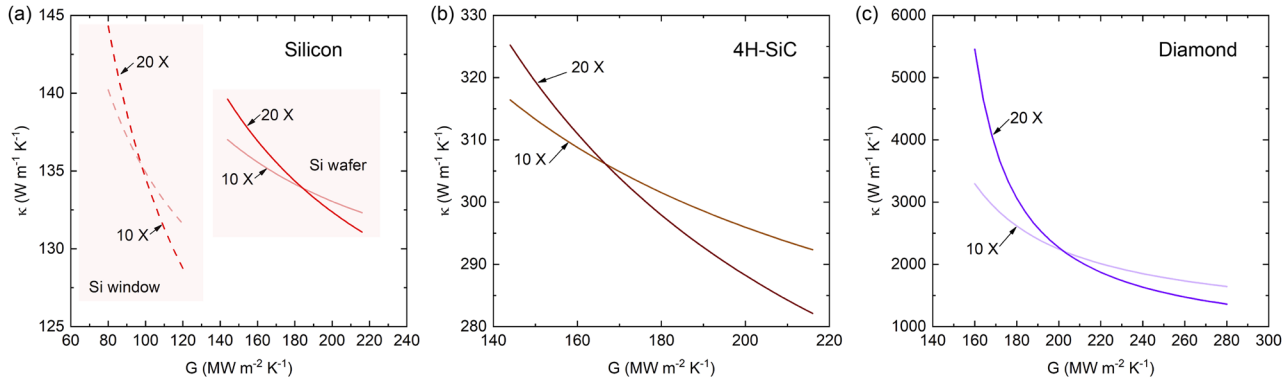

FIG. 8. Thermal conductivity, κ, vs. thermal boundary conductance, G, between the Al transducer and (a) silicon, (b) 4H–SiC, and (c) diamond. Two silicon samples were measured, a silicon wafer and silicon window, to show that the same thermal conductivity is obtained despite a large disparity in thermal boundary conductance between the two.

measured in this study. For Al_2O_3, sensitivity of the thermal model is overwhelmingly dictated by κ_2, demonstrating why Al_2O_3 is a great calibration sample to determine γ. For a-SiO_2, κ_2 again is the most sensitive parameter to our thermal model for the r_{01} used in the experiment. However, we see that sensitivity to $\kappa_{r,1}$ and d_1 is still somewhat significant. These two quantities (and their corresponding uncertainties) were measured via four point probe resistivity measurements and mechanical profilometry, respectively. Sensitivity to G (not shown) was not significant at all in this case.

For diamond, we see that for the r_{01} used in the experiment, we are highly sensitive to G. Therefore, in order to determine diamond's thermal conductivity, we need an accurate measurement for G. To obtain this quantity, we exploit the different sensitivities to κ_2 and G at different r_{01} values to determine both κ_2 and G. This procedure is performed for silicon (both the thin wafer and the thick window), 4H–SiC, and diamond. After determining $\Delta V/(V\,\Delta P)$ and converting to $\Delta T/\Delta|Q|$ via γ, we adjust G in the thermal model and determine the best fit κ_2. Repeating this procedure for two objective lenses results in two distinct curves describing κ_2 vs. G; the intersection of these curves represents the true values of κ_2 and G. This approach is similar to that described by Liu *et al.*[22] to extract both thermal conductivity and heat capacity in TDTR by using multiple modulation frequencies. The results are shown in Fig. 8 for (a) silicon, (b) 4H–SiC, and (c) diamond. For silicon, the thermal boundary conductances are different between the wafer and the window. This may be due to extrinsic effects such as roughness, surface finish, or variations in the native oxide thickness.[23] Nonetheless, the thermal conductivity is found to be equivalent in both samples, at ~135 W m^{-1} K^{-1}, in agreement with literature values.[24] Likewise, for 4H–SiC and diamond, we determine G and κ_2 based on the intersection of the curves for the 10× and 20× objectives. Note that this approach can be avoided by running experiments at larger pump/probe spot sizes to become insensitive to G entirely. This approach was not needed for any other samples studied since those measurements were not sensitive to thermal boundary conductance.

VI. RESULTS AND DISCUSSION

The measured thermal conductivities for all samples tested are listed in Table I. Results are shown for SSTR using

TABLE I. Best fit thermal conductivities for all samples tested using signal analysis by both the periodic waveform analyzer (PWA) and lock-in amplifier (LIA). For anisotropic materials, e.g., quartz and 4H–SiC, $\kappa \equiv \sqrt{\kappa_r \kappa_z}$.

	κ (W m^{-1} K^{-1})			
Sample	SSTR (PWA)	SSTR (LIA)	TDTR	Literature
a-SiO_2 glass slide	1.13 ± 0.08	1.06 ± 0.08	1.37 ± 0.13	1.3, Ref. 3
a-SiO_2 BK7 window	1.12 ± 0.08	1.07 ± 0.09	1.18 ± 0.10	1.06, Ref. 25
z-cut quartz	8.63 ± 0.36	8.63 ± 0.36	8.66 ± 0.61	8.6, Ref. 26
Al_2O_3 wafer	35.0 ± 1.4	35.2 ± 1.4	34.9 ± 1.6	34, Ref. 24
Al_2O_3 window	35.1 ± 1.4	34.8 ± 1.4	35.1 ± 1.8	34, Ref. 24
Silicon wafer	133 ± 6	136 ± 7	128 ± 9	133, Ref. 24
Silicon window	135 ± 10	136 ± 11	131 ± 9	133, Ref. 24
4H–SiC	310 ± 23	335 ± 28	324 ± 48	364, Ref. 27
Diamond	1760 ± 390	2010 ± 460	1950 ± 240	1900, Ref. 19

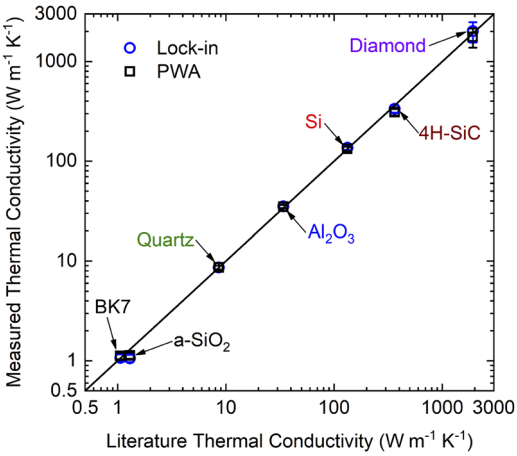

FIG. 9. Measured thermal conductivity vs. literature thermal conductivity. Results are shown for all samples using both the lock-in amplifier analysis (open circles) and periodic waveform analysis (open squares) methods. References are listed in Table I.

both the PWA/boxcar and LIA signal analysis approaches to reveal that the two approaches agree with one other. To confirm the accuracy of these measurements, Table I also shows the thermal conductivities for the same samples obtained using TDTR as well as reported thermal conductivities in the literature. Figure 9 shows the measured thermal conductivities vs. literature thermal conductivities spanning over three orders of magnitude. Overall, we observe excellent agreement between literature values and our measured thermal conductivities using both SSTR and TDTR. Because SSTR fundamentally measures $\sqrt{\kappa_z \kappa_r}$, for the case of anisotropic materials, the reported values for κ are equivalent to $\sqrt{\kappa_z \kappa_r}$. To obtain κ_z and κ_r independently in TDTR, for 4H–SiC, we followed the methodology outlined by Qian *et al.*,[27] using a relatively large pump diameter of ~20 μm and a high modulation frequency of 8.4 MHz to determine κ_z, followed by a smaller pump diameter of ~10 μm and a low modulation frequency of 1.0 MHz to determine κ_r. Using this approach, we find that κ_z = 299 ± 33 W m^{-1} K^{-1} and κ_r = 350 ± 64 W m^{-1} K^{-1}. Noting that the 4H–SiC sample measured in this study is N-doped at a level somewhere between 10^{18} and 10^{19} cm^{-3}, this measured κ_z agrees almost perfectly to that reported by Qian *et al.*,[27] whereas our measured κ_r is roughly 25% lower than the reported value. This difference could be due to the sample-specific attributes such as doping level or defects. Nonetheless, the measured κ for TDTR agrees well with that of SSTR. For quartz, the thermal diffusivity is too low to enable sensitivity to κ_r; instead, we determined κ with TDTR using two samples: z-cut and y-cut quartz. We find that for z-cut quartz, κ_z = 11.63 ± 0.80 W m^{-1} K^{-1}, while κ_z = 6.45 ± 0.46 W m^{-1} K^{-1} for y-cut quartz (equal to κ_r for z-cut quartz), both in agreement with values reported by Feser *et al.*[26] Thus, κ is equal to 8.66 ± 0.61 as determined by TDTR, in excellent agreement with that determined by SSTR.

One possible discrepancy between SSTR and literature is observed in the case of a-SiO$_2$. Although we reference a commonly accepted literature thermal conductivity for glass of 1.3 W m^{-1} K^{-1}, we note that reported values range from 1 to 1.4 W m^{-1} K^{-1} for glass depending on the chemistry and density; in our case, we measure a negligible difference between our glass microscope slide and our BK7 window. In TDTR, we measure 1.37 W m^{-1} K^{-1} for a-SiO$_2$, but because TDTR requires a known heat capacity to determine thermal conductivity, any discrepancy between our assumed value for volumetric heat capacity (1.66 MJ m^{-3} K^{-1}) and the actual value (which is density-dependent) could explain the difference in values obtained between the two techniques. To prove this point, TDTR and SSTR provide a similar thermal conductivity for BK7, but BK7 has a higher volumetric heat capacity than a-SiO$_2$.[25]

Finally, we note that the thermal conductivity of diamond has relatively large uncertainty. This is in part due to the limited temperature rise achievable in the material, resulting in a relatively low signal-to noise ratio. However, by taking multiple measurements at the same spot on the sample, we determine that this alone would only account for ~5%–10% of the uncertainty. Uncertainty in thermal boundary conductance adds another significant contribution, as revealed in Fig. 8. Finally, we note that there is significant variation between different spots on the sample; measured thermal conductivities varied as much as ~25% from the mean. This variation could be due to local thermal conductivity reduction from grain boundaries. Sood *et al.*[12] showed that local thermal conductivities in CVD-grown boron-doped polycrystalline diamond (an average grain size of 23 μm) can decrease κ by nearly 60% near grain boundaries. Because grain sizes in the diamond measured in this study range from 10 to 100 μm, we do not expect to see the same extent of variation observed by Sood *et al.*

VII. SOURCES OF UNCERTAINTY

Because SSTR relies on the proportionality constant, γ, it is highly important to characterize γ and its uncertainty with accuracy. To determine uncertainty in γ, we use a Monte Carlo approach to randomly vary input parameters to the thermal model based on their corresponding uncertainties. These parameters include the transducer thickness, d_1 (80 ± 3 nm); transducer thermal conductivity, $\kappa_{r,1}$ (100 ± 5 W m^{-1} K^{-1}); substrate thermal conductivity, κ_2 (for Al$_2$O$_3$, 35 ± 2 W m^{-1} K^{-1}); transducer/substrate thermal boundary conductance, G (for Al/Al$_2$O$_3$, 250 ± 30 MW m^{-2} K^{-1}); and effective radius, r_{01} (assumed 5% uncertainty). Additionally, we include experimental uncertainty in determining ($\Delta V/V\,\Delta P$). For the LIA analysis, this was determined by the standard deviation of the best fit slope to the experimental data, while in the PWA case, it was determined by the standard deviation of the signal in both the "on" and "off" states. Iterating over 10^5 simulations, we obtain a standard deviation of <5% of the mean. The same approach was used to characterize uncertainties of the samples tested in this study. Assuming the independence of parameters simplifies the uncertainty analysis so that the uncertainty is $\Delta \approx \sqrt{\sum_i \Delta_i^2}$, where Δ_i is the uncertainty in κ

resulting from uncertainty in the parameter i. The reported uncertainties are listed in Table I.

Signal noise comes primarily from $1/f$ noise. Using low probe powers, high pump powers, and longer averaging and/or lock-in times can help to overcome this noise, but ultimately there is a lower limit to the frequency that can be detected with a sufficient signal-to-noise ratio. We used a digital oscilloscope to observe, in the frequency domain, the magnitude of ΔV compared to the noise floor. For the highest pump powers used in each case, the signal-to-noise ratio was anywhere from 10 to 100. Lock-in amplification and/or boxcar averaging further facilitated signal extraction.

For uncertainty resulting from model parameters, sensitivity to these parameters dictates the magnitude of their contributions to total uncertainty. For low thermal conductivity materials, transducer thickness and thermal conductivity can be relatively significant, while for higher thermal conductivity materials, the interface conductance can be significant.

VIII. THIN FILM MEASUREMENT SENSITIVITY

While the discussion and experimental results have been focused on the measurement of bulk substrates, we note that thin film thermal conductivities can be measured under the right conditions. In Fig. 10, we show the relative sensitivities to thermal parameters of a three-layer model (layer 1: 80 nm transducer/layer 2: film/layer 3: substrate) as a function of layer 2 film thickness, assuming a 10× objective lens is used so that the pump and probe diameters are 20 μm (radii are 10 μm). Due to the sensitivity of SSTR measurements being highly dependent on the relative properties of film and substrate, κ_2 and κ_3 are varied in combinations of 1, 10, and 100 W m^{-1} K^{-1} for a total of nine cases. Sensitivities are shown for both in-plane (r) and cross-plane (z) directions as well as for transducer/film and film/substrate thermal boundary conductances (G_1 and G_2, respectively).

Quantifying the thickness at which SSTR can measure κ_2 as the thickness at which sensitivity to this parameter surpassing κ_3, we find that highly dissimilar κ_2 and κ_3 allow for such measurement as low as <100 nm, two orders of magnitude below the measurement characteristic length scale defined by the pump radius. Interestingly, whereas for bulk materials, SSTR maintains the same sensitivity to $\kappa_{r,2}$ and $\kappa_{z,2}$, for thin films, this is not the case. For a thermally conductive film on an insulating substrate, SSTR becomes highly sensitive to $\kappa_{r,2}$, whereas for a thermally insulating film on a conductive substrate, $\kappa_{z,2}$ becomes the dominant thermal parameter in the model. At the other extreme, when the film and the substrate κ are highly similar, sensitivity to κ_2 does not surpass κ_3 until close to 10 μm, i.e., the pump radius. In this case, symmetry in the temperature profile between the z and r directions is preserved so that sensitivity to κ_2 and κ_3 is equivalent,

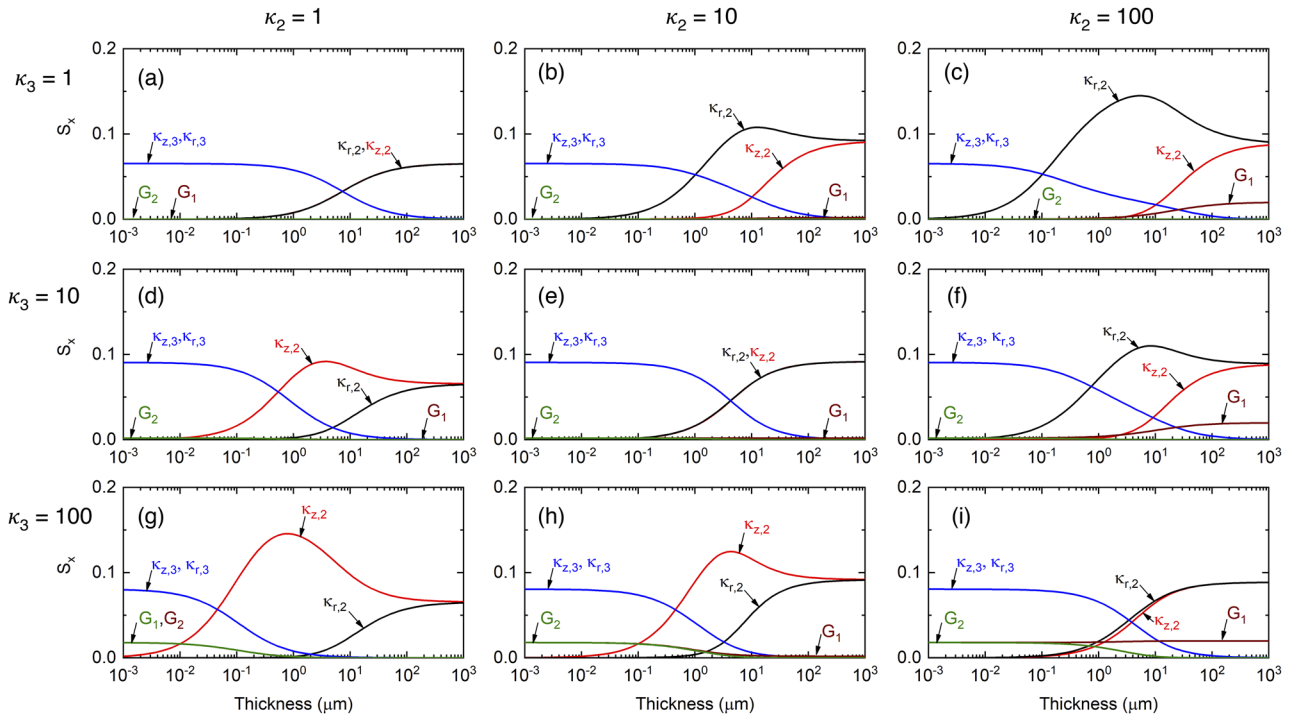

FIG. 10. Sensitivity to thermal parameters of a three-layer model (1: 80 nm transducer/2: film/3: substrate) vs. layer 2 film thickness. The nine cases considered include (a) κ_2 = 1, κ_3 = 1, (b) κ_2 = 10, κ_3 = 1, (c) κ_2 = 100, κ_3 = 1, (d) κ_2 = 1, κ_3 = 10, (e) κ_2 = 10, κ_3 = 10, (f) κ_2 = 100, κ_3 = 10, (g) κ_2 = 1, κ_3 = 100, (h) κ_2 = 10, κ_3 = 100, and (i) κ_2 = 100, κ_3 = 100 W m^{-1} K^{-1}. In all cases, the transducer thermal conductivity is set to 100 W m^{-1} K^{-1}, while the transducer/film and film/substrate thermal boundary conductances (G_1 and G_2, respectively) are set to 100 MW m^{-2} K^{-1}.

barring minor influence from G_2. Cleary, the measurement of thin films is facilitated by strong differences in the film and the substrate κ. Still, even in the worst-case scenario in which these thermal conductivities are equal, the critical film thickness that can be measured, as we define it, is about equal to the pump radius. Consequently, reducing the pump/probe radii via higher objective lenses becomes an option for improving sensitivity to thin film thermal conductivities.

IX. SUMMARY

A steady-state thermoreflectance method has been presented for measuring the thermal conductivity of materials. This method relies on square-wave modulation of a continuous wave pump laser to induce a steady-state temperature rise within a sample that is modulated continuously between "on" and "off" states. Using both a lock-in amplifier and periodic waveform analyzer with a boxcar averager, we measure the change in reflectivity of a sample via a continuous wave probe (proportional to temperature change) together with the change in power of the pump (proportional to heat flux). Using SSTR, we measure samples having thermal conductivities ranging from 1 to >2000 W m^{-1} K^{-1}.

ACKNOWLEDGMENTS

We appreciate funding from the Office of Naval Research, Grant No. N00014-15-1-2769. J.L.B. was supported by the Department of Defense (DoD) through the National Defense Science and Engineering Graduate Fellowship (NDSEG) Program.

APPENDIX A: MATHEMATICAL DESCRIPTION OF THE TRANSIENT TEMPERATURE RISE

In Ref. 15, we derived an expression to describe the surface temperature induced by a heating event with an arbitrary time-dependence. The temperature of the top surface as a function of radius and time, given by Eq. (23) in Ref. 15, is

$$T_{top}(r,t) = \frac{1}{2\pi}\int_{-\infty}^{\infty} \tilde{L}(r,\omega)\tilde{G}(\omega)e^{i\omega t}\,d\omega, \tag{A1}$$

where $\tilde{L}(r,\omega)$ is a function of radius, r, and angular frequency, ω. $\tilde{L}(r,\omega)$ incorporates the heating radius and material properties of the sample and $\tilde{G}(\omega)$ is the Fourier transform of the function describing the time dependence of the heat source. $\tilde{L}(r,\omega)$ is given by

$$\tilde{L}(r,\omega) = -\frac{1}{2\pi}\int_0^{\infty}\left(\frac{\tilde{\underset{\sim}{D}}(k,\omega)}{\tilde{\underset{\sim}{C}}(k,\omega)}\right)\exp\left(-\frac{k^2r_0^2}{8}\right)J_0(kr)\,k\,dk. \tag{A2}$$

Although given in Ref. 15, for the sake of completeness, we define $\tilde{\underset{\sim}{C}}$ and $\tilde{\underset{\sim}{D}}$, which are defined in the Hankel and frequency domains, based on the transfer matrix terms

$$\begin{bmatrix}\tilde{\underset{\sim}{A}}(k,\omega) & \tilde{\underset{\sim}{B}}(k,\omega)\\ \tilde{\underset{\sim}{C}}(k,\omega) & \tilde{\underset{\sim}{D}}(k,\omega)\end{bmatrix} = \prod_{i=n,n-1,\ldots}^{i=1}\mathbf{M}_i\mathbf{N}_i, \tag{A3}$$

$$\mathbf{M}_i = \begin{bmatrix}\cosh(q_iL_i) & -\frac{1}{q_i\kappa_z}\sinh(q_iL_i)\\ -q_i\kappa_z\sinh(q_iL_i) & \cosh(q_iL_i)\end{bmatrix}, \tag{A4}$$

$$\mathbf{N}_i = \begin{bmatrix}1 & -\frac{f(i)}{G_{i-1,i}}\\ 0 & 1\end{bmatrix}, \tag{A5}$$

$$f(i) = \begin{cases}1 & i \neq 1\\ 0 & i = 1\end{cases}, \tag{A6}$$

$$q_i^2 = \frac{1}{\kappa_{z,i}}(i\omega\rho_ic_{p,i} + \kappa_{r,i}k^2), \tag{A7}$$

where n is the number of layers in the material stack of the sample (for bulk materials with a transducer, this is two layers), L_i is the thickness of layer i, $G_{i-1,i}$ is the thermal boundary conductance between layers i and $i-1$, κ_z and κ_r are the through- and cross-plane thermal conductivities, respectively, ρ is the mass density, c_p is the specific heat capacity, and k is the Hankel transform variable. In this work, we follow the same procedure to determine the solution to the transient response but modify the surface heat flux boundary condition to start at time $t = 0$. To do so, we apply the Heaviside step function, $u(t)$, so that the source term for a CW source becomes

$$G(t) = A_0\,u(t), \tag{A8}$$

where A_0 is the absorbed power. The Fourier transform is

$$\tilde{G}(\omega) = A_0\pi\left(\frac{1}{i\pi\omega} + \delta(\omega)\right). \tag{A9}$$

Substituting Eq. (A9) into Eq. (A1), the surface temperature becomes

$$\begin{aligned}T_{top}(r,t) &= \frac{A_0}{2}\int_{-\infty}^{\infty}\tilde{L}(r,\omega)\left(\frac{1}{i\pi\omega} + \delta(\omega)\right)e^{i\omega t}\,d\omega\\ &= \frac{A_0}{2}\int_{-\infty}^{\infty}\frac{\tilde{L}(r,\omega)e^{i\omega t}}{i\pi\omega}\,d\omega + \frac{A_0}{2}\int_{-\infty}^{\infty}\tilde{L}(r,\omega)\delta(\omega)e^{i\omega t}\,d\omega\\ &= \frac{A_0}{2}\int_{-\infty}^{\infty}\frac{\tilde{L}(r,\omega)e^{i\omega t}}{i\pi\omega}\,d\omega + \frac{A_0}{2}\tilde{L}(r,0).\end{aligned} \tag{A10}$$

Integration is performed numerically. In order to simplify the integration procedure, we expand $\tilde{L}(r,\omega)$ so that the first term in Eq. (A10) becomes

$$\begin{aligned}&\frac{A_0}{2}\int_{-\infty}^{\infty}\frac{\tilde{L}(r,\omega)e^{i\omega t}}{i\pi\omega}\,d\omega\\ &= \frac{-A_0}{4\pi}\int_{-\infty}^{\infty}\left(\int_0^{\infty}\left(\frac{\tilde{\underset{\sim}{D}}(k,\omega)}{\tilde{\underset{\sim}{C}}(k,\omega)}\right)\exp\left(-\frac{k^2r_0^2}{8}\right)J_0(kr)\,k\,dk\right)\frac{e^{i\omega t}}{i\pi\omega}\,d\omega\\ &= \frac{-A_0}{4\pi}\int_0^{\infty}\left(\int_{-\infty}^{\infty}\left(\frac{\tilde{\underset{\sim}{D}}(k,\omega)}{\tilde{\underset{\sim}{C}}(k,\omega)}\right)\frac{e^{i\omega t}}{i\pi\omega}\,d\omega\right)\exp\left(-\frac{k^2r_0^2}{8}\right)J_0(kr)\,k\,dk\\ &= \frac{A_0}{4\pi}\int_0^{\infty}P_{\tilde{\underset{\sim}{t}}}(k,t)\exp\left(-\frac{k^2r_0^2}{8}\right)J_0(kr)\,k\,dk,\end{aligned} \tag{A11}$$

where $\underset{\sim}{P}_t$ is a time-dependent function defined by

$$\underset{\sim}{P}_t(k,t) = -\int_{-\infty}^{\infty}\left(\frac{\tilde{\underset{\sim}{D}}(k,\omega)}{\tilde{\underset{\sim}{C}}(k,\omega)}\right)\frac{e^{i\omega t}}{i\pi\omega}\,d\omega. \tag{A12}$$

The final term in Eq. (A10) can be shown to take a similar form so that

$$\frac{A_0}{2}\tilde{L}(r,0) = \frac{A_0}{4\pi}\int_0^{\infty}\underset{\sim}{P}_0(k)\exp\left(-\frac{k^2r_0^2}{8}\right)J_0(kr)\,k\,dk, \tag{A13}$$

where $\underset{\sim}{P}_0(k)$ is a time-independent function defined by

$$\underset{\sim}{P}_0(k) = -\int_{-\infty}^{\infty}\left(\frac{\tilde{\underset{\sim}{D}}(k,\omega)}{\tilde{\underset{\sim}{C}}(k,\omega)}\right)e^{i\omega t}\delta(\omega)\,d\omega = -\frac{\tilde{\underset{\sim}{D}}(k,0)}{\tilde{\underset{\sim}{C}}(k,0)}. \tag{A14}$$

The probe-averaged change in reflectance is the integration over the Gaussian intensity in real space. This probe averaged temperature rise, T_{PA}, is given by

$$T_{PA}(t) = \frac{4}{r_1^2}\int_0^{\infty}T_{top}(r,t)\exp\left(\frac{-2r^2}{r_1^2}\right)r\,dr. \tag{A15}$$

This expression can then be simplified to

$$\begin{aligned}
T_{PA}(t) &= \frac{4}{r_1^2}\int_0^{\infty}\left[\frac{A_0}{4\pi}\int_0^{\infty}\left(\underset{\sim}{P}_t(k,t)+\underset{\sim}{P}_0(k,t)\right)\exp\left(-\frac{k^2r_0^2}{8}\right)J_0(kr)\,k\,dk\right]\exp\left(\frac{-2r^2}{r_1^2}\right)r\,dr\\
&= \frac{A_0}{2}\int_0^{\infty}\left(\underset{\sim}{P}_t(k,t)+\underset{\sim}{P}_0(k,t)\right)\exp\left(-\frac{k^2r_0^2}{8}\right)\left[\frac{2}{\pi r_1^2}\int_0^{\infty}J_0(kr)\exp\left(\frac{-2r^2}{r_1^2}\right)r\,dr\right]k\,dk\\
&= \frac{A_0}{2}\int_0^{\infty}\left(\underset{\sim}{P}_t(k,t)+\underset{\sim}{P}_0(k,t)\right)\exp\left(-\frac{k^2r_0^2}{8}\right)\left[\frac{1}{2\pi}\exp\left(-\frac{k^2r_1^2}{8}\right)\right]k\,dk\\
&= \frac{A_0}{4\pi}\int_0^{\infty}\left(\underset{\sim}{P}_t(k,t)+\underset{\sim}{P}_0(k,t)\right)\exp\left(-\frac{k^2(r_0^2+r_1^2)}{8}\right)k\,dk.
\end{aligned} \tag{A16}$$

With P_0 and P_t defined above, it is straightforward to numerically integrate this expression to obtain the transient temperature rise.

APPENDIX B: FREQUENCY-DOMAIN AND STEADY-STATE TEMPERATURE RISE

The frequency domain solution to the temperature rise is given by[15]

$$T_{top}(r,\omega) = \tilde{L}(r,\omega)\tilde{G}(\omega). \tag{B1}$$

For an amplitude modulated CW laser heat source at frequency $\omega_0/2\pi$, $\tilde{G}(\omega) = A_0e^{i\omega_0 t} + A_1$, where A_0 is the amplitude of the modulated power absorbed by the sample, which is proportional to the power detected via pump lock-in detection, and A_1 is the average power absorbed. Since the lock-in technique relies on a periodic signal, we ignore the A_1 term in the subsequent equations. Furthermore, we assume lock-in amplification effectively rejects all other frequencies except the modulation frequency. Expanding Eq. (B1) and following the same procedure used in Eq. (A16), the probe-averaged temperature rise is

$$T_{top}(\omega_0) = -\frac{A_0}{2\pi}\int_0^{\infty}\frac{\tilde{\underset{\sim}{D}}(k,\omega_0)}{\tilde{\underset{\sim}{C}}(k,\omega_0)}\exp\left(-\frac{k^2(r_0^2+r_1^2)}{8}\right)k\,dk. \tag{B2}$$

The steady-state temperature rise is determined by setting $\omega_0 = 0$. As we showed in Fig. 2, as $\omega_0 \to 0$, the amplitude of temperature rise (proportional to the probe lock-in magnitude) approaches that of the steady-state temperature rise such that the steady-state condition may be assumed. However, for certain samples or experimentally limited spot sizes/frequencies, this assumption may not be true. Therefore, when determining thermal conductivity via the LIA approach, it is generally a good idea to include the nonzero experimental modulation frequency in the thermal model since even if the steady-state approximation is entirely valid, the model will still reflect this. For the PWA approach, however, we use a purely steady-sate model only ($\omega_0 = 0$) since the waveform is displayed in time to allow us to pick the regime of steady-state temperature rise.

REFERENCES

[1] M. J. Assael, K. D. Antoniadis, and W. A. Wakeham, Int. J. Thermophys. **31**, 1051 (2010).
[2] S. E. Gustafsson, Rev. Sci. Instrum. **62**, 797 (1991).
[3] D. G. Cahill, Rev. Sci. Instrum. **61**, 802 (1990).
[4] W. J. Parker, R. J. Jenkins, C. P. Butler, and G. L. Abbott, J. Appl. Phys. **32**, 1679 (1961).
[5] C. A. Paddock and G. L. Eesley, J. Appl. Phys. **60**, 285 (1986).
[6] A. J. Schmidt, R. Cheaito, and M. Chiesa, Rev. Sci. Instrum. **80**, 094901 (2009).
[7] D. Zhao, X. Qian, X. Gu, S. A. Jajja, and R. Yang, J. Electron. Packag. **138**, 040802 (2016).
[8] A. L. Pope, B. Zawilski, and T. M. Tritt, Cryogenics **41**, 725 (2001).
[9] J. Yang, C. Maragliano, and A. J. Schmidt, Rev. Sci. Instrum. **84**, 104904 (2013).
[10] M. Goni and A. J. Schmidt, J. Heat Transfer **138**, 020911 (2016).

[11]C. Wei, X. Zheng, D. G. Cahill, and J.-C. Zhao, Rev. Sci. Instrum. **84**, 071301 (2013).
[12]A. Sood, R. Cheaito, T. Bai, H. Kwon, Y. Wang, C. Li, L. Yates, T. Bougher, S. Graham, M. Asheghi, M. Goorsky, and K. E. Goodson, Nano Lett. **18**, 3466 (2018).
[13]L. Wang, R. Cheaito, J. L. Braun, A. Giri, and P. E. Hopkins, Rev. Sci. Instrum. **87**, 094902 (2016).
[14]J. Yang, E. Ziade, and A. J. Schmidt, J. Appl. Phys. **119**, 095107 (2016).
[15]J. L. Braun and P. E. Hopkins, J. Appl. Phys. **121**, 175107 (2017).
[16]V. Mishra, C. L. Hardin, J. E. Garay, and C. Dames, Rev. Sci. Instrum. **86**, 054902 (2015).
[17]Y. Wang, J. Y. Park, Y. K. Koh, and D. G. Cahill, J. Appl. Phys. **108**, 043507 (2010).
[18]R. B. Wilson, B. A. Apgar, L. W. Martin, and D. G. Cahill, Opt. Express **20**, 28829 (2012).
[19]C. M. Rost, J. Braun, K. Ferri, L. Backman, A. Giri, E. J. Opila, J.-P. Maria, and P. E. Hopkins, Appl. Phys. Lett. **111**, 151902 (2017).
[20]J. L. Braun, C. J. Szwejkowski, A. Giri, and P. E. Hopkins, J. Heat Transfer **140**, 052801 (2018).
[21]T. Favaloro, J. H. Bahk, and A. Shakouri, Rev. Sci. Instrum. **86**, 024903 (2015).
[22]J. Liu, J. Zhu, M. Tian, X. Gu, A. Schmidt, and R. Yang, Rev. Sci. Instrum. **84**, 034902 (2013).
[23]P. E. Hopkins, L. M. Phinney, J. R. Serrano, and T. E. Beechem, Phys. Rev. B **82**, 085307 (2010).
[24]R. B. Wilson and D. G. Cahill, Appl. Phys. Lett. **107**, 203112 (2015).
[25]M. J. Assael, S. Botsios, K. Gialou, and I. N. Metaxa, Int. J. Thermophys. **26**, 1595 (2005).
[26]J. P. Feser, J. Liu, and D. G. Cahill, Rev. Sci. Instrum. **85**, 104903 (2014).
[27]X. Qian, P. Jiang, and R. Yang, Mater. Today Phys. **3**, 70 (2017).